Water Science & Technology

IWA PUBLISHING

Water Science & Technology Vol 84 No 3, 596 doi: 10.2166/wst.2021.255

Catalytic wet peroxide oxidation degradation of magenta wastewater and preparation of FeOCl/montmorillonite

Tiancheng Hun, Binxia Zhao*, Tingting Zhu, Linxue Liu, Zhiliang Li and Li Sun
School of Chemical Engineering, Northwest University, Xi'an 710069, Shaanxi, China
*Corresponding author. E-mail: zhaobx@nwu.edu.cn

TH, 0000-0002-4729-6393

ABSTRACT

The iron oxychloride/pillared montmorillonite (FeOCl/MMT) catalyst was prepared by wet impregnation method and solid melting method. Various characterization techniques were used to analyze the microscopic morphology and structure of a series of catalysts. Moreover, the catalysts were used to treat magenta-simulated dye wastewater through catalytic wet peroxide oxidation (CWPO) degradation. The magenta removal rate and chemical oxygen demand (COD) removal rate of the magenta-simulated dye wastewater were used to evaluate the catalytic performance of the catalyst, and the optimal catalyst preparation conditions were selected. The results showed that the solid melting method was more favorable to the preparation of the catalyst, and the COD removal rate of wastewater can reach 70.8% when the FeOCl load was 3%. Moreover, 96.2% of the magenta in the solution was removed. The COD removal rate of the magenta wastewater decreased by only 12.4% after the catalyst was repeatedly used six times, indicating that the catalyst has good activity and stability. The Fermi equation can simulate the reaction process of the catalyst treating magenta wastewater at high temperature.

Key words: Fenton reactions, Fermi equation, iron oxychloride, montmorillonite, wastewater treatment

HIGHLIGHTS

- Loading FeOCl on montmorillonite with Al-pillar support to treat magenta-simulated wastewater.
- Determining the optimal preparation conditions of the catalyst and finding that only a small amount of Fe ions leached in repeat experiments.
- The mechanism of the CWPO reaction was explored, and the free radical groups that play an important role in the reaction was found.

GRAPHICAL ABSTRACT

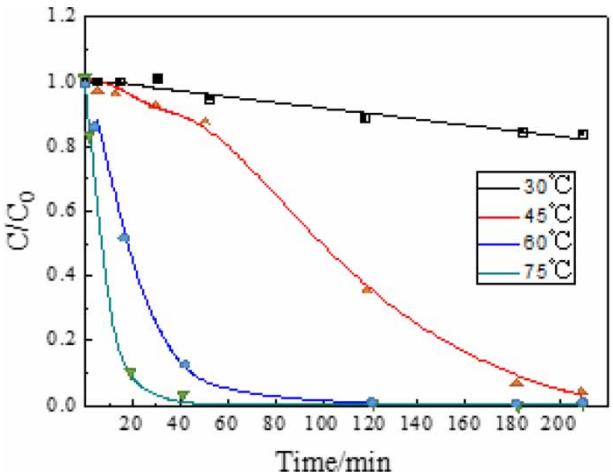

1. INTRODUCTION

In recent years, due to the increase in demand for textile products, the dye and dyeing industry has developed rapidly. If the untreated dye wastewater is discharged into rivers, it will appear deep reddish-purple due to the azo dye with high biological oxygen demand (BOD) and chemical oxygen demand (COD). If the ratio of BOD/COD is between 0.2 and 0.5, the dyeing wastewater contains a large amount of non-biodegradable matter in nature (Pello *et al.* 2018). The dye wastewater can cause serious environmental and health problems; magenta is the main component of dye wastewater (Tang *et al.* 2014). Catalytic wet peroxide oxidation (CWPO) technology is an important method to degrade organic wastewater. Hydrogen peroxide (H_2O_2) is used as an oxidant in CWPO technology, and the H_2O_2 is decomposed by the catalyst to form hydroxyl radicals (HO·) (Molina *et al.* 2010). HO· with a high oxidation potential of 2.8 V can attack many toxic organic pollutants, and it can mineralize them into carbon dioxide, water, and harmless inorganic substances (Wang *et al.* 2019). CWPO reaction has been extensively studied in recent years, and the developed heterogeneous catalyst can be used and recovered in a wider pH range (pH = 3.0–9.0), which overcomes the limitation of homogeneous catalyst, thereby making the process simpler and solving the problem of secondary pollution (Molina *et al.* 2010).

Metal oxides that can change valence are widely distributed in nature with abundant reserves and strong oxidizing properties, and they are useful for the degradation of organic matter (Malhotra *et al.* 2014). Iron oxychloride (FeOCl) is an important Fenton catalyst. From Table S1, the HO· generation rate constant over FeOCl was as high as $2.93 \times 10^{-4}\ s^{-1}$, which was 1–3 orders of magnitude higher than other iron-based materials. When the rate constant was normalized to the unit surface area, it was found that it decomposes H_2O_2 more efficiently, and its HO· generation rate was 2–4 orders of magnitude higher than traditional iron-based materials. This shows excellent performance in degrading persistent organic compounds (Yang *et al.* 2013; Sun *et al.* 2018b). FeOCl has a unique iron coordination environment, including Fe(II)–O, Fe(III)–O, Fe–Cl and Fe–Fe, and a large number of unsaturated iron atoms are exposed on the plane (020). FeOCl has excellent catalytic performance due to its unique structure. It has been proven that when Fe(III) in FeOCl is inserted or reacted with other species, it is easily reduced to Fe^{2+} (Luo *et al.* 2019).

Montmorillonite (MMT) is a smectic clay; every layer is composed of an Al-based octahedral plate sandwiched between two tetrahedral silicate plates. Researchers found that high mechanical strength, good thermal stability, a porous and a large specific surface area are the advantages of MMT (Chetverikova *et al.* 2019). Catrinescu *et al.* used Al-pillared clay as a high surface area carrier and prepared Fe-loaded Al–Fe–pillared clay as a catalyst for the 4-chlorophenol CWPO reaction. The degradation rate and total organic carbon removal rate of 4-chlorophenol were 100% and 52%, respectively (Tian *et al.* 2011).

In this paper, Al-pillared MMT loaded FeOCl was used as the catalyst. Al exists in the MMT layer in the form of Al_{13} polycation, and it was calcined to form the Al_2O_3 'oxidation column'. Al-pillared MMT can be a good catalyst carrier due to its large layer spacing and specific surface area. At the same time, the FeOCl loaded on the pillared MMT will decompose H_2O_2 through Fe(III) on the polar surface to produce HO·, to accelerate the decomposition of pollutants (Tian *et al.* 2005).

Finding the best preparation conditions (preparation method and FeOCl loading) of the catalyst, testing the stability of the catalyst, exploring the reaction mechanism, and selecting the appropriate equation to simulate the reaction are the main goals in the paper.

2. EXPERIMENTAL

2.1. Catalyst preparation

1 g acid-modified MMT was added to 30 mL $AlCl_3{\cdot}6H_2O$ solution ($0.4\ mol{\cdot}L^{-1}$). The mixture was stirred vigorously at 80 °C for 10 min, and then 5 mL polyethylene glycol (PEG-400) was added to the solution. After stirring for 5 min, 75 mL NaOH solution($0.4\ mol{\cdot}L^{-1}$) was dropped into the reaction solution through a dropping funnel at a rate of 1 mL min^{-1} and stirred vigorously so that the molar ratio of $[OH^-]/[Al^{3+}]$ was 2.5:1 (Guo *et al.* 2004). After dropping, the mixture was continuously stirred for 2 h. After ageing for 12 h at 60 °C, the precipitate was centrifuged and washed six times until it did not contain Cl^-. The precipitate was dried for 24 h at 60 °C, then it was calcined in an air atmosphere at 400 °C for 2 h to obtain Al-pillared MMT.

The catalysts were prepared by the equal volume impregnation method and the solid melting method, respectively (Shih *et al.* 2003). The impregnated loaded catalyst was prepared by an equal volume impregnation method. The specific

synthesis steps are as follows: first, weighing a certain amount of Al-pillared MMT and determining its saturated water absorption; second, weighing the corresponding $FeCl_3{\cdot}6H_2O$ according to the amount of FeOCl loaded and calculating the reaction equation to produce iron oxychloride, as shown in Equation (1). The $FeCl_3{\cdot}6H_2O$ was dissolved in the water, added to the Al-pillared montmorillonite, and stirred continously to allow sufficient impregnation. Finally, the obtained impregnated material was dried at 60 °C and calcined at 220 °C for 2 h. This was recorded as FeOCl/MMT(s). Another catalyst was synthesized by solid melting method. The specific preparation process is as follows: weighing a certain mass of $FeCl_3{\cdot}6H_2O$ and mixing it mechanically with the Al-pillared montmorillonite in a mortar for 10 min until the powder becomes lemon yellow. This mixture was also calcined at 220 °C for 2 h, and recorded as FeOCl/MMT(g).

$$FeCl_3 \cdot 6H_2O \rightarrow HCl + FeOCl + 5H_2O \quad (1)$$

2.2. Catalyst characterization

The structural parameters of the catalysts were determined by N_2 adsorption/desorption isotherms measured on the surface area and pore size analyzer (NOVE 2200e, Quantachrome). The setting test conditions were: the samples were pretreated at 160 °C for 18 h and then tested at −196 °C. The crystal structures of the samples were analyzed using an X-ray diffractometer (SmartLab SE, Rigaku). The test conditions were: Cu-Kα radiation at 40 kV and 30 mA, scanning speed 0.1°/s, scanning range 5–80°. The microscopic morphology and structure of the sample were analyzed using scanning electron microscope (SEM) ZEISS SIGMA, Carl Zeiss). A small amount of the sample was dispersed on the surface of the conductive tape, then scanned and observed after spraying gold. The molecular group of the sample was measured by Fourier infrared spectroscopy (IRTffinity-1S, Shimadzu). The test conditions were: no tablet forming was required, but the sample was fully dried; the sample scan wavenumber was 400–4,000 cm^{-1}. The catalysts were analyzed using an UV–Vis spectrophotometer (UV-2600, Shimadzu). Using barium sulfate as the reference, the wavelength scanning range was 200–800 nm.

2.3. Catalytic activity experiment

0.05 g catalyst was put in to a three-necked flask. Then, 100 mL magenta-simulated dye wastewater (200 $mg{\cdot}L^{-1}$) was poured into the flask, pH was adjusted to 3 and the mixture was stirred for 30 min to reach adsorption equilibrium. The H_2O_2/magenta ratio was controlled to 60:1; the reaction time was controlled to 210 min; samples at different times were taken to test and analyze the COD removal rate and the magenta removal rate in the water sample.

2.4. Analytical method

2.4.1. Determination of magenta solution concentration

The standard magenta solution with concentrations of 0, 0.5, 5, 10, 20, and 40 $mg{\cdot}L^{-1}$ were prepared, and their absorbances at the maximum absorption wavelength (543 nm) measured. From the obtained absorbance of samples with different concentrations, the fitting curve was obtained to obtain the fitting formula. The fitting curve is shown in Fig. S1. Equation (2) is the fitting formula:

$$C = 20.9A_x + 0.36 \quad (2)$$

where A_x indicates the absorbance at 543 nm; C is the concentration of the magenta solution.

After that, the absorbance of the magenta solution was measured at different times during the reaction, and the concentration of the magenta solution was calculated by the fitting formula.

2.4.2. Determination of COD

The amount of organic matter in the magenta solution can be expressed by COD, which is measured using the potassium dichromate method. Details of the potassium dichromate method are provided in the Supplementary Material. The

calculation formula of the COD removal rate of magenta solution is shown in Equation (3):

$$\eta_{COD} = \frac{COD_0 - COD_t}{COD_O} \times 100\% \quad (3)$$

where COD_0 indicates the beginning COD value of the mixture; and COD_t is the COD value of mixture at t.

3. RESULTS AND DISCUSSION

3.1. Characterization of the catalyst

The N_2 adsorption/desorption isotherms of samples prepared with unpillared MMT and different loading methods are shown in Figure 1. From Figure 1, it can be seen that FeOCl/MMT(g) samples, FeOCl/MMT(s) samples, and the original MMT all belong to type IV isotherms. All of them have the characteristic performance of mesopores. It shows that the mesoporous structure of the original MMT of FeOCl/MMT(g) and FeOCl/MMT(s) samples were not destroyed during the pillaring and loading process. At low relative pressure ($P/P_0 < 0.4$), N_2 adsorption on the surface of the sample forms a monolayer. At moderate relative pressure ($0.4 < P/P_0 < 0.5$), N_2 continued to adsorb to form a multi-molecular layer. At high relative pressure ($P/P_0 > 0.5$), the capillary was condensed (Sun *et al.* 2014). The adsorption process of mesoporous materials usually shows adsorption–desorption hysteresis, which will lead to the formation of H3 hysteresis loops, indicating that the accumulation of nanosheets in the sample had formed slit holes (Gao *et al.* 2014).

Also, the relevant sample structure parameters are listed in Table 1. The specific surface area, pore size, and pore volume of FeOCl/MMT(g) and FeOCl/MMT(s) samples supported by metal ions and loaded are significantly increased, and the d_{001} value increased from 1.235 nm of unpillared MMT to 1.441 nm and 1.524 nm, respectively. On the one hand, it shows that Al_2O_3 successfully pillared the layered structure of MMT. On the other hand, it shows that a small amount of active component FeOCl exists on the surface or between layers of the sample in oligomers, forming a new pore structure (Li *et al.* 2020). It shows that FeOCl can be used as an active component in the MMT layer, and it can also stabilize the carrier structure. Among them FeOCl/MMT(g) has a larger specific surface area ($S_{BET} = 141\ m^2 \cdot g^{-1}$) compared with FeOCl/MMT(s), increasing by 6%. The pore diameter (D_{med}) increased from 3.02 nm to 3.41 nm, and the total pore volume (V_{total}) increased from 0.137 cm^3/g to 0.156 cm^3/g. FeOCl/MMT(g) may therefore exhibit higher catalytic performance.

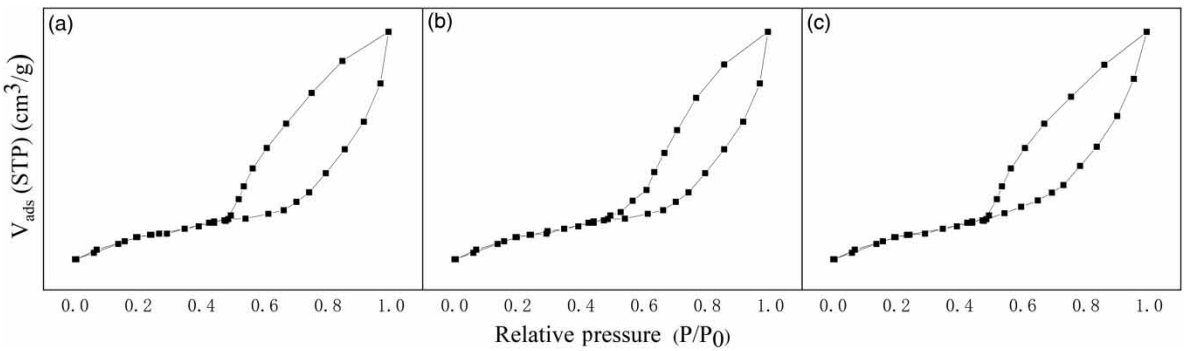

Figure 1 | N_2 adsorption–desorption curves of samples with different loading methods: (a) MMT; (b) FeOCl/MMT(g); (c) FeOCl/MMT(s).

Table 1 | Structural parameters of different samples

Sample	S_{BET} ($m^2 \cdot g^{-1}$)	S_{mic} ($m^2 \cdot g^{-1}$)	V_{mic} ($cm^2 \cdot g^{-1}$)	V_{total} ($cm^3 \cdot g^{-1}$)	D_{med} (nm)	d_{001} (nm)
MMT	54	31	0.061	0.117	2.68	1.235
FeOCl/MMT(g)	141	117.4	0.072	0.156	3.41	1.524
FeOCl/MMT(s)	133	112.6	0.066	0.137	3.02	1.441

Note: S_{mic}, micropore surface area; V_{mic}, micropore volume; d_{001}, interplanar spacing of 001 crystal plane.

The elemental analysis of samples prepared with MMT and different loading methods are shown in Table 2. The element content of FeOCl/MMT(g) and FeOCl/MMT(s) samples are different from unpillared MMT. On the one hand, this can be attributed to the fact that cation exchange during the pillaring process causes a large number of metal Al ions to enter the MMT layer, resulting in the decrease of Na, Mg, K, Ca, and Si contents in the sample, indicating the success of pillared MMT (Wu *et al.* 2020). On the other hand, the content of Fe increased in the subsequent loading. Moreover, FeOCl/MMT(g) has a higher Fe content than FeOCl/MMT(s), indicating that the solid melting method may be more beneficial to load FeOCl on MMT (Kong *et al.* 2010).

X-ray diffraction (XRD) spectra of samples prepared with MMT and different loading methods are shown in Figure 2; the d_{001} values were listed in Table 1. From Figure 2, the spectra of FeOCl/MMT(g) and FeOCl/MMT(s) catalysts were similar to the unpillared MMT, indicating that the layered structure of the original MMT was not destroyed.

The original montmorillonite (001) crystal plane diffraction peak signal was at $2\theta = 9.4°$. The characteristic diffraction peaks of the FeOCl/MMT(s) and FeOCl/MMT(g) catalysts moved at $2\theta = 6.2°$, indicating that Al ions had successfully entered between the MMT layers, which confirmed that the carrier MMT was successfully pillared. Also, the XRD peaks of FeOCl/MMT(s) and FeOCl/MMT(g) catalysts at $2\theta = 37.9°$, 35.6°, 25.9°, and 10.6° corresponding to {111}, {021}, {110}, {010} crystal planes are consistent with pure FeOCl crystal (JCPDS No.72-0619), indicating that both loading methods can convert $FeCl_3{\cdot}6H_2O$ into FeOCl and load it on MMT. However, due to the higher peak intensity of FeOCl/MMT(g) here, it exhibits higher crystallinity and better catalytic activity. According to Scherrer's equation, calculating the size of FeOCl crystals in FeOCl/MMT(g) is about 50 nm (Schnleber *et al.* 2015).

Figure 3 shows scanning electron micropscopy (SEM) spectra of samples prepared with unsupported MMT and different loading methods. It was found that unpillared MMT has a curled layered structure from Figure 3(a), which was made up of

Table 2 | Element content of different samples

	Element content (wt%)						
Sample	**Na**	**Mg**	**K**	**Ca**	**Si**	**Al**	**Fe**
MMT	1.17	3.81	1.65	12.06	65.36	15.95	–
FeOCl	–	–	–	–	–	–	55.55
FeOCl/MMT(g)	1.08	2.87	1.02	7.23	60.12	18.15	9.53
FeOCl/MMT(s)	1.02	2.85	1.15	7.98	62.17	17.95	6.88

Note: The mass of all samples is 0.05 g.

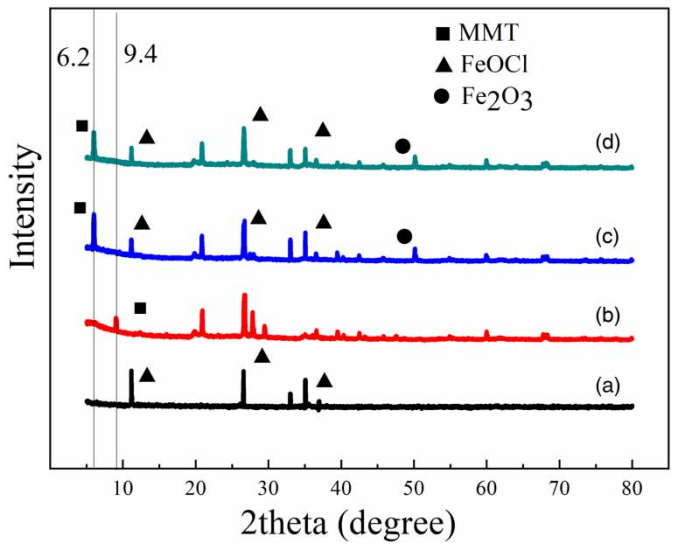

Figure 2 | XRD spectra of samples with different loading methods: (a) FeOCl/MMT(s); (b) FeOCl/MMT(g); (c) MMT; (d) FeOCl.

irregular agglomeration of plate-like particles formation. Figure 3(b) shows that pure FeOCl is a coral-like structure formed by random stacking of plate-shaped nanosheets. Figure 3(c) and 3(d) shows that the structure of FeOCl/MMT(g) and FeOCl/MMT(s) samples is similar to the original MMT structure, indicating that the layered structure of MMT was not destroyed during the pillar support and load process (Zhang *et al.* 2019). Also, in the FeOCl/MMT(g) catalyst in Figure 3(c), flat FeOCl crystals were observed on the surface of the carrier MMT. However, there were no obvious FeOCl crystals observed in the FeOCl/MMT(s) catalyst in Figure 3(d).

The catalysts prepared by different loading methods were treated with the same CWPO method to treat magenta-simulated dye wastewater. The COD removal rate of magenta wastewater changes with time, as shown in Fig. S2. It can be found that FeOCl/MMT(g) has a positive effect on COD compared with FeOCl/MMT(s); the removal rate of COD increased by 13.3%. The COD removal rate and magenta removal rate of the two catalysts are shown in Table 3, the catalytic effect of FeOCl/MMT(g) is better than that of FeOCl/MMT(s). The removal efficiencies expressed as COD are smaller than those obtained

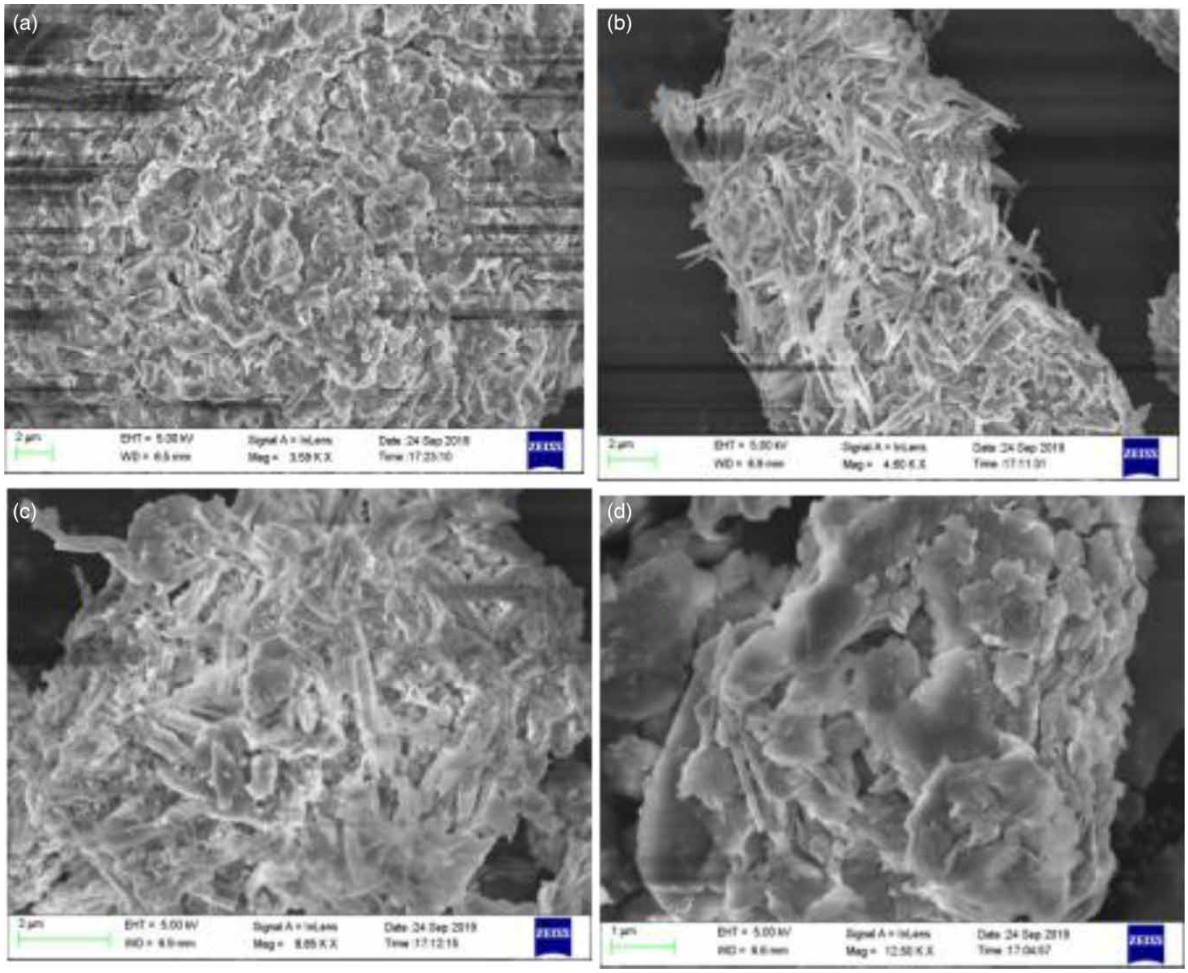

Figure 3 | SEM of samples with different loading methods: (a) MMT; (b) FeOCl; (c) FeOCl/MMT(g); (d) FeOCl/MMT(s).

Table 3 | COD removal rate and magenta removal rate after the reaction

Catalyst	COD removal rate	Magenta removal rate
FeOCl/MMT(g)	61.9%	96.2%
FeOCl/MMT(s)	48.6%	82.3%

for magenta, confirming that magenta oxidation occurs in multiple steps and results in several by-products, which are more resistant to oxidation than the initial pollutant (Catrinescu *et al.* 2011).

According to the above analysis, the solid melting method is more suitable for removing magenta in wastewater.

In the CWPO reaction, FeOCl formed by $FeCl_3{\cdot}6H_2O$ conversion was the active component. Loading the proper amount of $FeCl_3{\cdot}6H_2O$ on the carrier formed more FeOCl to enhance the catalytic effect. Therefore, a series of *x*-FeOCl/MMT(g) samples with different loadings of FeOCl were prepared, where *x* represents the mass ratio of FeOCl to unsupported MMT, which were 1%, 3%, and 5%, respectively. The optimal FeOCl loading was selected through characterization analysis.

The Fourier-transform infrared spectroscopy (FT–IR) spectra of pure FeOCl and samples with different loadings are shown in Figure 4. In Figure 4, we can see similar unpillared MMT characteristic peaks that were observed in the FT–IR spectra of samples prepared with different loadings. The absorption peak at 3,622 cm^{-1} corresponds to the –OH stretching vibration of the bound water and adsorbed water between the MMT layers. Its deformation vibration appeared at wavelength 1,746 cm^{-1}. The peak at 1,006 cm^{-1} is the peak of deformation vibration of MMT Si–O–Si. The peak at 434 cm^{-1} is the peak of deformation vibration of Si–O–Al formed by the Al ion entering the MMT layer (Pratiwi *et al.* 2017). The –OH was removed from the MMT carrier to form Si–O–Si and Si–O–Al bonds during the pillared heating process, indicating that the MMT is successfully pillared (Zhang *et al.* 2018). At 3,622 cm^{-1} and 1,746 cm^{-1} in the FT-IR spectrum of *x*-FeOCl/MMT(g) sample, the peaks of the –OH stretching vibration and deformation vibration at the position were blue-shifted. Also, the faint vibration peaks of Fe–O and Fe–Cl were observed from the FT-IR spectrum of *x*-FeOCl/MMT(g) sample at 670 cm^{-1} and 1,596 cm^{-1}, which means that the active component FeOCl was produced in different loadings. Moreover, the peak intensities were different due to different loadings (Scully *et al.* 2010).

The UV–Vis spectra of pure FeOCl and samples with different loadings are shown in Figure 5. The transition absorption band of $t_1 \rightarrow t_2$ and $t_1 \rightarrow e^-$ of Fe^{3+} were observed at $\lambda = 230$ nm and $\lambda = 270$ nm at the spectral lines. A weak absorption peak belonging to the polymeric iron oxide cluster $(FeO)_n$ appeared at an external wavelength of 550 nm. The intensity of this absorption peak continued to increase with the increase of FeOCl loading (Merli *et al.* 2015). The existential form of iron depended on the amount of FeOCl loading, so when the loading was increased to 5%, high loading increases the formation of oligomeric iron, and affects the catalytic activity of the sample (Abd-El-Aziz *et al.* 1995).

The *x*-FeOCl/MMT(g) samples prepared with different FeOCl loadings were used as catalysts to degrade the magenta solution. Figure 6 shows the COD removal rate of the magenta solution over time, and Table 4 shows the COD removal rate and magenta removal rate after the reaction. When only MMT was used to degrade magenta solution, the COD removal rate was only 21.2%. The COD removal rate when only MMT was used is close to the COD removal rate when only H_2O_2 was used (Figure 7), indicating that MMT does not have a catalytic effect in this experiment. When FeOCl was loaded on MMT, the COD removal rate increases. This may be because MMT provides more active sites and makes FeOCl more evenly distributed. All catalysts (except MMT) show a high removal rate of magenta (Sun *et al.* 2014). When the loading was 3%, it can

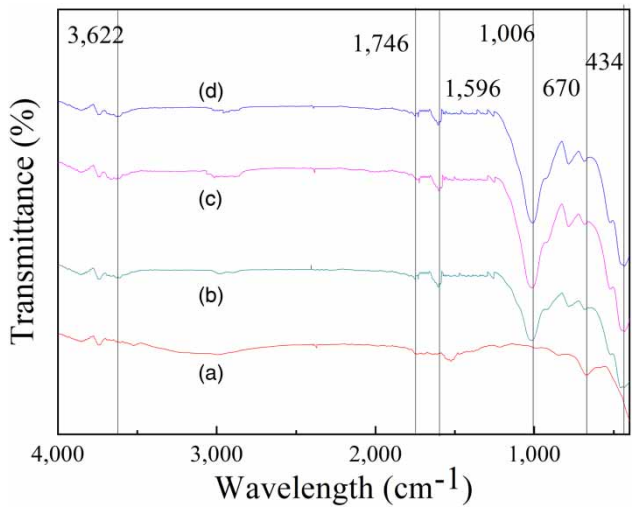

Figure 4 | FT-IR spectra of samples with different loadings: (a) FeOCl; (b) 1%-FeOCl/MMT(g); (c) 3%-FeOCl/MMT(g); (d) 5%-FeOCl/MMT(g).

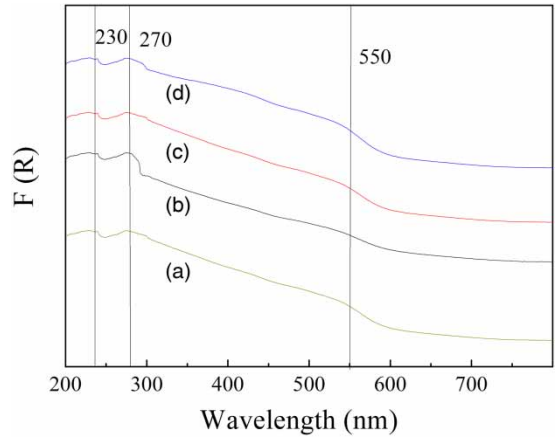

Figure 5 | UV–Vis spectra of samples with different loadings: (a) FeOCl; (b) 1%-FeOCl/MMT(g); (c) 3%-FeOCl/MMT(g); (d) 5%-FeOCl/MMT(g).

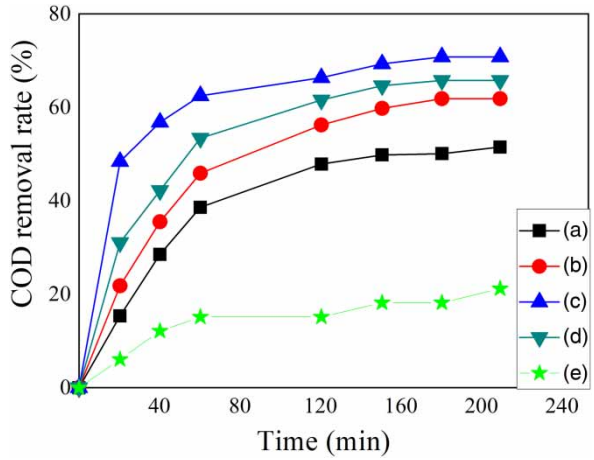

Figure 6 | COD spectra of samples with different loadings: (a) FeOCl; (b) 1%-FeOCl/MMT(g); (c) 3%-FeOCl/MMT(g); (d) 5%-FeOCl/MMT(g); (e) MMT. Experiment conditions: 200 mg/L^{-1} of magenta, 1g L^{-1} of catalyst, 0.38 mL of H_2O_2, 60 °C, pH = 3.0.

Table 4 | COD removal rate and magenta removal rate after the reaction

Catalyst	COD removal rate	Magenta removal rate
FeOCl	51.5%	70.2%
1%-FeOCl/MMT(g)	61.9%	85.2%
3%-FeOCl/MMT(g)	70.8%	96.2%
5%-FeOCl/MMT(g)	65.8%	91.4%
MMT	21.2%	53.1%

provide enough active sites to degrade dye wastewater well. However, when the loading exceeded 3%, the COD removal rate dropped slightly. This may because the formation of too much FeOCl caused an agglomeration behavior, which is not conducive to the dispersion of active components on the surface of the carrier. Some FeOCl may even enter the pores of the carrier and block some pore channels, resulting in a decrease in the molecules diffusion rate of reactants and products (Biddinger *et al.* 2011). The data demonstrates that 3%-FeOCl/MMT(g) was not only the most active for magenta but also the most efficient catalyst for COD removal.

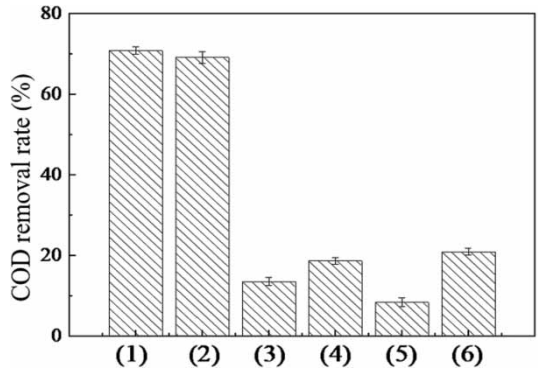

Figure 7 | COD removal rate of different systems: (1) catalyst + H_2O_2; (2) catalyst + H_2O_2 + benzoquinone; (3) catalyst + H_2O_2 + tert-butanol; (4) catalyst + H_2O_2 + potassium iodide; (5) catalyst; (6) H_2O_2. Experiment conditions: 200 mg·L^{-1} of magenta, 1 g·L^{-1} of catalyst, 0.38 ml L^{-1} of H_2O_2, 60 °C, pH = 3.0.

3.2. Study on the stability of the catalyst

Table 5 shows the COD removal rate of the magenta solution was only reduced by 12.4% after the catalyst was reused six times, suggesting that the catalyst maintains a high activity. However, it also indicated that a large amount of accumulation of intermediate products in the catalyst might block the pores, or it was due to the recovery and excessive heating treatments so that the active component FeOCl in the catalyst was polymerized (Tagliabue *et al.* 2004). Also, according to the dissolution data of total Fe ions, it can be found that as the reaction proceeds successively, the amount of total Fe ions dissolved gradually decreases. It showed that the active metal content on the catalyst surface was reduced, and the FeOCl nanoparticles existing between the catalyst layers were more stable. The quality of total Fe ions leaching showed that the active components of the catalyst were less lost (Bailón-García *et al.* 2013).

3.3. Study on CWPO degradation reaction mechanism and kinetics of magenta dye wastewater

In the process of CWPO degradation of the magenta solution, benzoquinone (BQ) and tert-butanol (TBA) were added as free radical scavengers to inhibit the main oxidation groups $\cdot O_2^-$ and HO· in the process of free radical reaction (Buc-Calderon & Roberfroid 1988). Potassium iodide (KI) was used to inhibit HO· and $\cdot O_2^-$ on the catalyst surface (Ali *et al.* 2021). We explored the active groups that play a major role in the CWPO reaction system and set up six different reaction systems: (1) catalyst + H_2O_2; (2) catalyst + H_2O_2 + BQ; (3) catalyst + H_2O_2 + TBA; (4) catalyst + H_2O_2 + KI; (5) catalyst; (6) H_2O_2.

Figure 7 shows the effect of different active group trapping agents on the COD removal rate of the CWPO reaction system. There were significant differences in the COD removal rate of the magenta solution in different reaction systems.

According to the change of COD removal rate of systems (1)–(3), it can be seen that HO· plays an important role in the reaction. Comparing system (3) and system (4), the contribution of free HO· was dominant in the CWPO reaction system. However, the surface HO· also contributed. When only the catalyst was added in system (5), the COD removal rate was the lowest. From the aforementioned characterization and analysis, it can be seen that the catalyst has a large specific surface area and can adsorb organic pollutants. In system (6), only H_2O_2 was added, and the COD removal rate was about 20%. This is because H_2O_2 has an oxidizing effect and can degrade a small amount of magenta (Yang *et al.* 2019).

Table 5 | Experimental results of CWPO

Sample	COD removal rate (%)	Quality of total Fe ions leaching (mg·L^{-1})
1	70.8	0.732
2	66.4	0.140
3	63.5	0.129
4	61.2	0.109
5	59.5	0.105
6	58.4	0.103

CWPO reaction is a typical free radical reaction, including adsorption, surface reaction, and desorption process (Chen *et al.* 2016). First, macromolecular organics are adsorbed on the surface of the catalyst or enter the active sites inside the catalyst due to molecular diffusion. Moreover, the active sites of the catalyst are dense; thereby the HO· reaction is triggered, as in Equations (4)–(7). After reaching the adsorption equilibrium, the strong oxidizing group HO· oxidize to degrade organic pollutants to generate a series of intermediate products and low-molecular compounds as in Equation (7). The catalytic cycle begins after the surface reaction, where the reaction induction period is the key step (Dang *et al.* 2010).

$$Fe^{3+} + H_2O_2 \rightarrow Fe^{2+} + HOO\cdot + H^+ \quad (4)$$

$$Fe^{3+} + HOO\cdot \rightarrow Fe^{2+} + HOO\cdot + H^+ \quad (5)$$

$$Fe^{2+} + H_2O_2 \rightarrow Fe^{3+} + OH^- + HO\cdot \quad (6)$$

$$HO\cdot + \text{compounds} \rightarrow \text{intermediates} \rightarrow CO_2 + H_2O \quad (7)$$

Kwan & Voelker proved that the decomposition of H_2O_2 and the degradation of organic compounds mainly occur on the surface of Fe_2O_3 (Kwan & Voelker 2003). Voinov *et al.* found that specific catalytic sites on the surface of nano-scale γ-Fe_2O_3 are at least 50 times more efficient in the production of HO· than Fe ions (Voinov *et al.* 2011). The polar surface (especially the 020 plane) in the basic structure of FeOCl is filled with a large number of unsaturated Fe atoms. These Fe atoms are uniformly arranged on the plane in the O–Fe–Cl configuration so that the polarization plane has a greater affinity for H_2O_2 molecules (Sun *et al.* 2018a). Therefore, the excellent catalytic effect of FeOCl/MMT in the reaction is attributed to the fact that FeOCl in the catalyst can decompose H_2O_2 in a short time to generate a large number of hydroxyl radicals. First, when H_2O_2 and organic pollutants are adsorbed, Fe on the polarized surface of FeOCl acts as the reaction center for the activation and decomposition of H_2O_2. The electrophilic Cl and O may increase the reduction potential of Fe, and the self-oxidation–reduction potential of FeOCl can promote and pass the hydrogen oxide reactions to produce $\cdot HO_2$. Moreover, Fe^{3+} is rapidly reduced to Fe^{2+}. The resulting Fe^{2+} reacts with H_2O_2 to form HO·, the rate of generation of HO· on Fe^{2+} is 3–4 orders of magnitude higher than that on Fe^{3+}. The HO· then attacks organic compounds. Finally, the redox cycle of the Fe^{2+}/Fe^{3+} pair is completed, and the redox cycle is considered to be the essence of the Fenton reaction (Sun *et al.* 2018b; Luo *et al.* 2019). Figure S3 shows this process.

The traditional semi-empirical general model will have the following problems when simulating CWPO reaction kinetics: (1) the relationship between the reaction time in the early stage of induction and the concentration of reactants is not linear; and (2) the reaction rate between the induction phase and the activation phase is very different. For the oxidation reaction of Fe-based heterogeneous catalysts with H_2O_2, the pollutants generally degrade slowly at the beginning and then rapidly degrade, and the pollutant concentration shows a lying S shape over time (Taghdiri *et al.* 2013). This paper therefore used the Fermi function as a kinetic model to establish the mathematical relationship between reaction conditions and rate constants (Li *et al.* 2010). The Fermi equation was used to describe the CWPO reaction kinetics of the magenta solution, as shown in Equation (8):

$$\frac{C}{C_0} = \frac{1}{1 + \exp[k(t - t_{1/2})]} \quad (8)$$

where k is the apparent rate constant; t is the reaction time; $t_{1/2}$ is the time used when the reactant conversion rate was 50%; C is the concentration of pollutants at time t; and C_0 is the initial concentration of pollutants.

Figure 8 shows the degradation process of magenta at different temperatures. C/C_0 is the ratio of the concentration of magenta at time t to the initial concentration. The relevant data are listed in Table 6. It can be seen that the fitting curves of 60 °C and 75 °C had the same changing trend; the curve was a lying S shape, the magenta degradation efficiency was close to 100% after 120 min of reaction, and the linear correlation values (R^2) were above 0.99. Both of them had the basic conditions for fitting with the Fermi equation. However, when the temperature was low (45 °C and 30 °C), it was not suitable to use the Fermi equation to simulate them. This is because the induction period of the reaction was too long when the temperature was low (Peleg 2010).

When the reaction temperature was high, this reaction was suitable for simulation with the Fermi function. Moreover, the reaction rate constants were 0.1726 min^{-1} for 60 °C and 0.2987 min^{-1} for 75 °C. At high temperatures, the catalyst

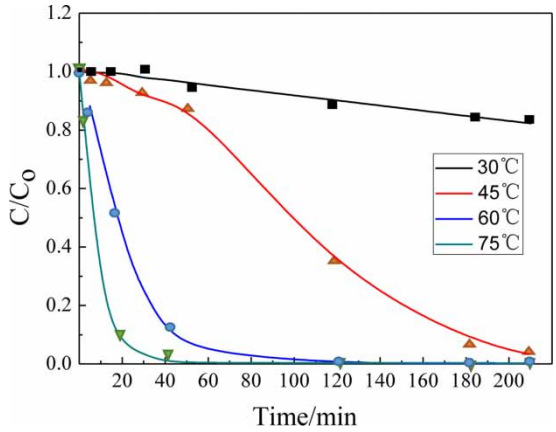

Figure 8 | Degradation process of magenta at different temperatures.

Table 6 | Fermi equation dynamic fit results

Temperature	K (min^{-1})	$t_{1/2}$ (min)	R^2
30 °C	–	336.3	0.9374
45 °C	–	92.55	0.9912
60 °C	0.1726	21.45	0.9973
75 °C	0.2987	15.37	0.9991

performance was excellent. When there was a reaction induction period at the beginning of the reaction, the reaction speed was slow, and the catalyst surface was activated, but it was not uniform. Only a small amount of HO· was generated. After the reaction induction period, the reaction entered a pseudo-steady state stage when the concentration of H_2O_2 continuously decreased and the decomposition to produce HO· accelerated, speeding up the oxidation rate (Gordon & Marsh 2009; Sang *et al.* 2011).

4. CONCLUSION

FeOCl/MMT was used as catalyst, H_2O_2 as an oxidant, and a heterogeneous CWPO reaction was used to treat magenta wastewater. The reaction occurred easily and, it could be carried out at 60 °C. The highly active and stable FeOCl/MMT catalyst is the key to affecting the CWPO reaction rate. The 3%-FeOCl/MMT(g) catalyst was selected after optimizing the preparation conditions to degrade the magenta solution. The specific surface area of this catalyst is 141 $m^2\ g^{-1}$, which has a relatively high specific surface area. The catalyst still had a high catalytic activity after six uses. The synthesis method of the FeOCl catalyst is simple, and it can effectively promote the generation of HO·. The fitting results show that the Fermi equation can describe the degradation process of magenta at high temperatures. Therefore, the catalyst provides a new opportunity for the CWPO method to degrade magenta water pollutants.

ACKNOWLEDGEMENT

This work was supported by the key research and development program of Shaanxi, China (2018GY-067).

DATA AVAILABILITY STATEMENT

All relevant data are included in the paper or its Supplementary Information.

REFERENCES

Abd-El-Aziz, A. S., de Denus, C. R., Zaworotko, M. J. & MacGillivra, L. R. 1995 Controlled design of oligomeric ethers with pendant cyclopentadienyliron moieties. *Journal of the Chemical Society* **24**, 3375–3393.

Ali, M., Zhang, X., Idrees, A., Tariq, M., Danish, M., Farooq, U., Shan, A., Jiang, X., Huang, J. & Lyu, S. 2021 Advancement in Fenton-like reactions using PVA coated calcium peroxide/FeS system: pivotal role of sulfide ion in regenerating the Fe(II) ions and improving trichloroethylene degradation. *Journal of Environmental Chemical Engineering* **9**, 104591.

Bailón-García, E., Maldonado-Hódar, F., Pérez-Cadenas, A. & Carrasco-Marín, F. 2013 Catalysts supported on carbon materials for the selective hydrogenation of citral. *Catalysts* **3**, 853–877.

Biddinger, E. J., Deak, D. V., Singh, D., Marsh, H., Tan, B., Knapke, D. S. & Ozkan, U. S. 2011 Examination of catalyst loading effects on the selectivity of CNx and Pt/VC ORR catalysts using RRDE. *Journal of the Electrochemical Society* **158**, B402.

Buc-Calderon, P. & Roberfroid, M. 1988 Inhibition of O2-.- and HO.- mediated processes by a new class of free radical scavengers: the *N*-acyl dehydroalanines. *Free Radical Research Communications* **5**, 159–168.

Catrinescu, C., Arsene, D. & Teodosiu, C. 2011 Catalytic wet hydrogen peroxide oxidation of para-chlorophenol over Al/Fe pillared clays (AlFePILCs) prepared from different host clays. *Applied Catalysis B* **101**, 451–460.

Chen, H., Lee, J., Zheng, Y. & Duan, Q. 2016 A non-traditional energy transfer process in CWPO heterogeneous reaction for wastewater treatment. *Chemical Engineering Research* **114**, 142–147.

Chetverikova, A. G., Filyak, M. M. & Kanygina, O. N. 2019 Influence of high-frequency microwave radiation on montmorillonite structure parameters. *Cermica* **65**, 635–640.

Dang, T. H., Lesaint, O. & Denat, A. 2010 Efficiency of several pulsed discharge types to degrade organic pollutants in water. *Annual Report Conference on Electrical Insulation and Dielectic Phenomena* **1**, 1–4.

Gao, Y., Li, W., Sun, H., Zheng, Z., Cui, X., Wang, H. & Meng, F. 2014 A facile in situ pillaring method – the synthesis of Al-pillared montmorillonite. *Applied Clay Science* **88–89**, 228–232.

Gordon, T. R. & Marsh, A. L. 2009 Temperature dependence of the oxidation of 2-Chlorophenol by hydrogen peroxide in the presence of goethite. *Catalysis Letters* **132**, 349–354.

Guo, X. K., Liu, Q. H. & Lin, Q. C. 2004 Preparation of La-modified Cu-based Al-Ce pillared montmorillonite and its catalytic properties for selective reduction of NO by propylene. *Chinese Journal of Catalysis* **25**, 989–994.

Kong, Q., Hu, Y., Song, L., Wang, Y. & Fan, W. 2010 Influence of Fe-MMT on crosslinking and thermal degradation in silicone rubber/clay nanocomposites. *Polymers for Advanced Technologies* **17**, 463–467.

Kwan, W. P. & Voelker, B. M. 2003 Rates of hydroxyl radical generation and organic compound oxidation in mineral-catalyzed Fenton-like systems. *Environmental Science Technology* **37**, 1150.

Li, L., Chen, P. & Gloyna, E. F. 2010 Generalized kinetic model for wet oxidation of organic compounds. *AIChE Journal* **37**, 1687–1697.

Li, J., Chen, Y., Yang, X., Gao, S. & Cao, R. 2020 Visible-light-mediated high-efficiency catalytic oxidation of sulfides using wrinkled c_3n_4 nanosheets. *Journal of Catalysis* **381**, 579–589.

Luo, J., Sun, M., Ritt, C. L., Liu, X., Pei, Y., Crittenden, J. C. & Elimelech, M. 2019 Tuning Pb(II) adsorption from aqueous solutions on ultrathin iron oxychloride (FeOCl) nanosheets. *Environmental Science Technology* **53**, 2075–2208.

Malhotra, S., Chen, H., Dew, E. R. W., Haywood, E. L. & Richardson, G. 2014 Integration of non-noble DRAM electrode. United States Patent No. 8652927-B2.

Merli, M., Sciascia, L., Pavese, A. & Diella, V. 2015 Modelling of thermo-chemical properties over the sub-solidus MgO–FeO binary, as a function of iron spin configuration, composition and temperature. *Physics and Chemistry of Minerals* **42**, 347–362.

Molina, C. B., Zazo, J. A., Casas, J. A. & Rodriguez, J. J. 2010 CWPO of 4-CP and industrial wastewater with Al-Fe pillared clays. *Water Science and Technology: A Journal of the International Association on Water Pollution Research* **61**, 2161–2168.

Peleg, M. 2010 A model of microbial growth and decay in a closed habitat based on combined Fermi's and the logistic equations. *Journal of the Science of Food and Agriculture* **71**, 225–230.

Pello, A. M., Judy, L., Madeleine, B., Ralph, C., Caryn, J., David, O. & Devendra, S. 2018 A combined activated sludge-filtration-ozonation process for abattoir wastewater treatment. *Journal of Water Process Engineering* **25**, 157–163.

Pratiwi, M. I., Afifah, N. & Saleh, R. 2017 Fe-doped ZnO supported with montmorillonite: synthesis, characterization, and photocatalytic activity. *IOP Conference Series: Materials Science and Engineering* **202**, 012038.

Sang, K. H., Hwang, T. M., Yoon, Y. & Kang, J. W. J. C. 2011 Evidence of singlet oxygen and hydroxyl radical formation in aqueous goethite suspension using spin-trapping electron paramagnetic resonance (EPR). *Chemosphere* **84**, 1095–1101.

Schnleber, A., Zhang, J., Van Smaalen, S., Reuvekamp, P. G., Kremer, R. K. & Senyshyn, A. 2015 A magnetic order and crystal structure of FeOCl described in superspace. *Acta Crystallographica Section A Foundations and Advances* **71** (a1), s394–s394.

Scully, S. F., Bissessur, R., Dahn, D. C. & Xie, G. 2010 In situ polymerization/intercalation of substituted anilines into iron(III) oxychloride. *Solid State Ionics* **181**, 933–938.

Shih, K. Y., Carney, M. J. & Denton, D. A. 2003 Metallocene and constrained geometry catalyst systems employing agglomerated metal oxide/clay support-activator and method of their preparation. United States Patent No. 6559090-B1.

Sun, T., Zhao, B. X., Wang, Q., Sun, Y. & Zhang, X. L. 2014 Preparation of Fe-Zr-pillared montmorillonite catalysts for treating dye wastewater by its catalytic wet peroxide oxidation. *Gao Xiao Hua Xue Gong Cheng Xue Bao* **28**, 659–664.

Sun, M., Chu, C., Geng, F., Lu, X. & Kim, J. H. 2018a Reinventing Fenton chemistry: iron oxychloride nanosheet for pH-Insensitive H_2O_2 activation. *Environmental Science & Technology Letters* **5**, 186–191.

Sun, M., Zucker, I., Douglas, M. D., Zhou, X., Qu, J. & Elimelech, M. 2018b Reactive, self-cleaning ultrafiltration membrane functionalized with iron oxychloride nanocatalysts. *Environmental Science & Technology* **52**, 8674–8683.

Taghdiri, M., Saadatjou, N., Zamani, N. & Farrokhi, R. 2013 Heterogeneous degradation of precipitated hexamine from wastewater by catalytic function of silicotungstic acid in the presence of H_2O_2 and H_2O_2/Fe^{2+}. *Journal of Hazardous Materials* **246–247**, 206–212.

Tagliabue, M., Carati, A., Flego, C., Millini, R., Perego, C., Pollesel, P., Stocchi, B. & Terzoni, G. 2004 Study on the stability of a Ga/Nd/ZSM-5 aromatisation catalyst. *Applied Catalysis A General* **265**, 23–33.

Tang, X., Li, J., Mao, Y., Xu, N., Jin, J., Wang, M. & Liu, Y. 2014 Dye wastewater treatment using composite catalysts in catalytic wet peroxide oxidation. *Environmental Chemistry* **33**, 341–348.

Tian, C., Ma, Z. & Zeng, F. 2005 Effect of OH-/Al^{3+} ratio on the properties of Al-pillared montmorillonite. *Bulletin of the Chinese Ceramic Society* **24**, 32–36, 41.

Voinov, M. A., Sosa, P. J. O., Morrison, E., Smirnova, T. I. & Smirnov, A. I. 2011 Surface-mediated production of hydroxyl radicals as a mechanism of iron oxide nanoparticle biotoxicity. *Journal of the American Chemical Society* **133**, 35–41.

Wang, J., Cao, Z. F., Ren, H., Yu, C. & Zhong, H. 2019 Reactivation of Fenton catalytic performance for Fe_3O_4 catalyst: optimizing the cyclic performance by low voltage electric field. *Applied Surface Science* **500**, 144045.

Wu, K., Ye, Q., Wu, R. & Dai, H. 2020 Alkali metal-promoted aluminum-pillared montmorillonites: high-performance CO_2 adsorbents. *Journal of Solid State Chemistry* **291**, 121585.

Yang, X. J., Xu, X. M., Xu, J. & Han, Y. F. 2013 Iron oxychloride (FeOCl): an efficient Fenton-like catalyst for producing hydroxyl radicals in degradation of organic contaminants. *Journal of the American Chemical Society* **135**, 16058.

Yang, G., Mo, S., Xing, B., Dong, J. & Yuan, J. 2019 Effective degradation of phenol via catalytic wet peroxide oxidation over N, S, and Fe-tridoped activated carbon. *Environmental Pollution* **258**, 113687.

Zhang, M., Chen, X., Zou, H. & Qianqian, L. I. 2018 Ultrasonic assisted Al–Zn pillared montmorillonite and its adsorption of Coomassie brilliant blue. *Textile Auxiliaries* **35**, 27–29, 64.

Zhang, S.-P., Yu, C., Bai, S.-Q. & Liu, R.-P. 2019 Catalytic degradation of rhodamine B by FeOCl activated hydrogen peroxide. *Huanjing Kexue* **40**, 5009–5014.

First received 29 March 2021; accepted in revised form 18 June 2021. Available online 1 July 2021